A 140-GHz FMCW TX/RX-Antenna-Sharing Transceiver With Low-Inherent-Loss Duplexing and Adaptive Self-Interference Cancellation

Xibi Chen, *Student Member, IEEE*, Xiang Yi, *Senior Member, IEEE*, Muhammad Ibrahim Wasiq Khan, *Student Member, IEEE*, Xingcun Li, *Student Member, IEEE*, Wenhua Chen, *Senior Member, IEEE*, Jianfeng Zhu, *Student Member, IEEE*, Yang Yang, *Senior Member, IEEE*, Kenneth E. Kolodziej, *Senior Member, IEEE*, Nathan M. Monroe, *Student Member, IEEE*, and Ruonan Han, *Senior Member, IEEE*

***Abstract*—This article presents a 140-GHz frequency-modulated continuous-wave (FMCW) radar transceiver featuring transmit/receive (TX/RX) antenna sharing that address a TX/RX beam misalignment problem when large-aperture lenses/mirrors/reflectarrays are used for pencil beam forming. A full-duplexing technique based on circular polarization and geometrical symmetry is applied to mitigate the 3 dB + 3 dB insertion loss inherent to conventionally adopted directional couplers, while still maintaining high TX-to-RX isolation. In addition, a self-adaptive self-interference cancellation (SIC) is implemented to suppress extra leakage due to antenna mismatch from a desired frontside radiation scheme. The TX/RX antenna sharing enables the pairing with a large 3-D printed planar lens and boosts the measured effective isotropic radiated power (EIRP) to 25.2 dBm. The measured total radiated power and minimum single-sideband noise figure (SSB NF) including antenna and duplexer losses are 6.2 dBm and 20.2 dB, respectively. The measured total TX-RX isolation is 33.3 dB under 14-GHz wide FMCW chirps. Based on a 65-nm complimentary metal–oxide–semiconductor (CMOS) technology, the chip has a die area of 3.1 mm^2 and consumes 405 mW of dc power. Among all reported sub-THz transceivers with TX/RX antenna sharing, this work demonstrates the highest total radiated power and is the only work that has >30 dB of TX-RX isolation while mitigating the inherent 6 dB coupler loss.**

***Index Terms*—Angular resolution, complimentary metal–oxide–semiconductor (CMOS), frequency-modulated continuous-wave (FMCW), full-duplex, monostatic radar, self-interference cancellation (SIC), terahertz (THz), transmit/receive (TX/RX) antenna sharing.**

I. Introduction

HIGH-resolution integrated radars are crucial in nowadays' automotive, vital sign, and security sensing applications [1], [2], [3]. Radars operating in the microwave and low-millimeter-wave regimes [3], [4], [5], [6], [7] require large aperture size to achieve high angular resolution, for example, a 24-GHz radar requires $\sim 60 \times 60$-cm^2 aperture area to realize 1° beamwidth. In addition, ranging resolution is also limited by the small absolute bandwidth. LiDARs [8], [9], [10], while providing excellent resolution, cannot operate reliably in environments with degraded visual (e.g., cloudy, rainy, etc.) conditions [11], [12], [13] or strong light interference. In comparison, the sub-terahertz/terahertz (sub-THz/THz) spectrum shows great opportunities in both high-resolution and all-weather radar imaging capabilities. In [14], a 260-GHz complimentary metal–oxide–semiconductor (CMOS) reflectarray with a size of 5.4×5.4 cm^2 enables imaging with 1° angular resolution in both azimuth and elevation. In [15], a CMOS frequency-modulated continuous-wave (FMCW) radar scanning from 220 to 320 GHz delivers 1.5-mm ranging resolution.

For isolation between the radar transmitter (TX) and the receiver (RX), bistatic configuration[1] with separate TX and RX antenna positions is commonly adopted [16], [17], [18], [19], [20]. However, in non-MIMO high-angular resolution systems, the radar transceiver should pair with a large-size lens/reflector for beam collimation. The bistatic arrangement then causes severe misalignment between the peaks of TX

[1]Single-chip radars with separate TX and RX antennas are sometimes also considered as "monostatic" due to the small absolute separation value. Here, we still refer those as "bistatic" and use phrases "TX/RX antenna sharing" and "monostatic" interchangeably.

Manuscript received 11 April 2022; revised 10 July 2022; accepted 16 August 2022. This article was approved by Associate Editor Hiroyuki Ito. An earlier version of this paper was presented in part at the IEEE Solid-State Circuits Conference (ISSCC), San Francisco, CA, USA, in February 2022 [DOI: 10.1109/ISSCC42614.2022.9731637]. *(Corresponding author: Xibi Chen.)*

Xibi Chen, Muhammad Ibrahim Wasiq Khan, Nathan M. Monroe, and Ruonan Han are with the Department of Electrical Engineering and Computer Science, Massachusetts Institute of Technology (MIT), Cambridge, MA 02139 USA (e-mail: xibichen@mit.edu; ruonan@mit.edu).

Xiang Yi was with the Department of Electrical Engineering and Computer Science, Massachusetts Institute of Technology (MIT), Cambridge, MA 02139 USA. He is now with the School of Microelectronics, South China University of Technology, Guangzhou 511442, China.

Xingcun Li was with the Department of Electrical Engineering and Computer Science, Massachusetts Institute of Technology (MIT), Cambridge, MA 02139 USA. He is now with the Department of Electronic Engineering, Tsinghua University, Beijing 100084, China.

Wenhua Chen is with the Department of Electronic Engineering, Tsinghua University, Beijing 100084, China.

Jianfeng Zhu and Yang Yang are with the School of Electrical and Data Engineering, University of Technology Sydney, Ultimo, NSW 2007, Australia.

Kenneth E. Kolodziej is with the MIT Lincoln Laboratory, Lexington, MA 02421 USA.

Color versions of one or more figures in this article are available at https://doi.org/10.1109/JSSC.2022.3202814.

Digital Object Identifier 10.1109/JSSC.2022.3202814

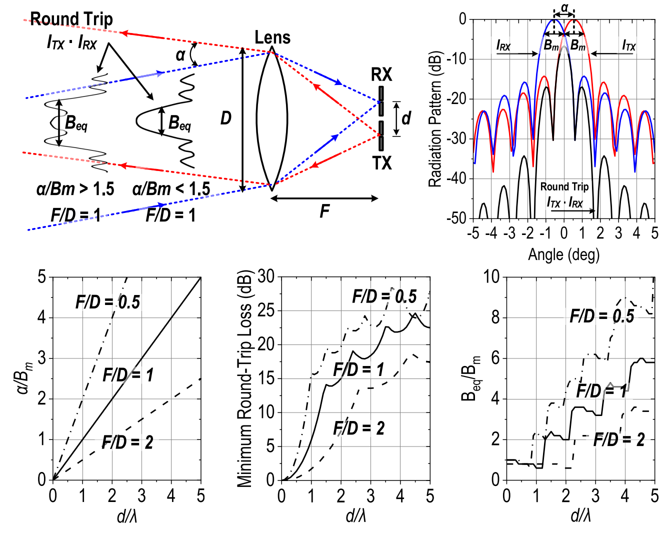

Fig. 1. Misalignment of TX and RX beams in bistatic radars.

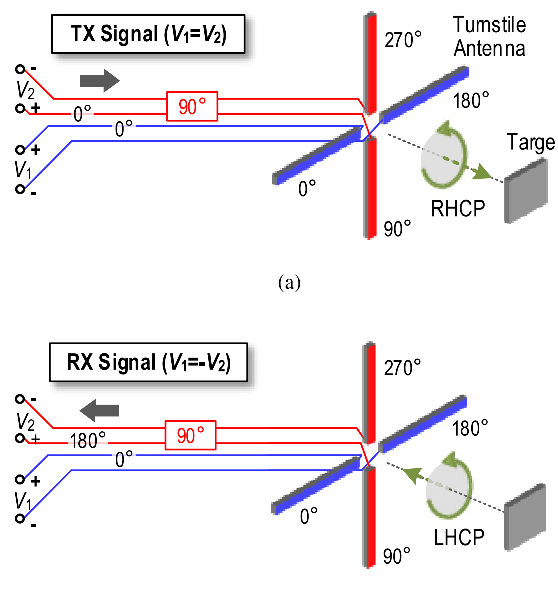

(a)

(b)

Fig. 2. Principles of CP waves for duplexing. (a) RHCP TX wave with a common-mode stimulus at V_1 and V_2 ports. (b) LHCP RX wave with differential outputs at V_1 and V_2 ports.

and RX beam patterns, $I_{\mathrm{TX}}(\theta, \phi)$, and $I_{\mathrm{RX}}(\theta, \phi)$ (see Fig. 1), which from geometrical optics [21] can be quantified as

$$\frac{\alpha}{B_m} \approx C \tan^{-1}\left(\frac{d}{F}\right)\frac{D}{\lambda} \approx C\,\frac{d/\lambda}{F/D} \tag{1}$$

where α is the angle between the TX and RX beams, B_m is the 3-dB angular beamwidth, $d \ll F$ is the distance between TX and RX antennas, C is a constant that relates to aperture shape, and F and D are the focal length and diameter of the optics, respectively. Since $I_{\mathrm{TX}}(\theta, \phi) \cdot I_{\mathrm{RX}}(\theta, \phi)$ determines the overall imager response, the above misalignment not only broadens the equivalent imaging spot size (B_{eq} in Fig. 1), but also causes link budget loss. The numerical calculation in Fig. 1, assuming a square optical aperture (or $C \approx 1$) with a typical $F/D = 1$, shows that an antenna separation of only one wavelength already leads to a misalignment α equal to the formed beamwidth B_m and 6-dB round trip loss. A similar situation was reported in [22], where a 4-mm TX and RX antenna separation at 122 GHz causes a 6° beam misalignment, which is larger than the width of the collimated beam with 29-dBi directivity.

Radar transceivers with a shared TX and RX antenna (ANT) interface, or monostatic configuration, are therefore required in the above scenario. However, to isolate the FMCW TX and RX signals, a circulator or a directional/hybrid coupler is normally required [4], [5], [6], [7], [23], [24], [25], [26], [27], [28]; however, the former is not suitable for on-chip integration and operations above 100 GHz, and the latter typically leads to an inherent 3-dB insertion loss in the TX-to-ANT path, and another inherent 3-dB loss in the ANT-to-RX path [25], [26]. With the unavoidable impedance mismatch (hence signal reflection) at the ANT interface, the degraded TX-to-RX isolation also often causes problems including, but not limited to, receiver saturation and excessive amplitude/phase noise. In [29], the aforementioned inherent coupler insertion loss is mitigated through two sets of hybrid couplers and a quad-feed circularly polarized antenna. However, the achieved 26 dB isolation relies on excellent antenna matching enabled by backside radiation through a silicon lens, which increases cost and packaging complexity.

This article presents a 140-GHz 65-nm CMOS monostatic radar transceiver, which was originally reported in [30]. It not only circumvents the 6-dB inherent insertion loss of couplers, but also facilitates low-cost and packaging-complexity frontside radiation through an adaptive self-interference cancellation (SIC). In Section II, basic principles of our techniques are given. Then, Section III provides design details of the on-chip antenna and some key circuit blocks. In Section IV, electrical performances of the transceiver chip are characterized. The chip achieves 33.3 dB of total TRX isolation under 14-GHz-wide FMCW chirps, and total radiated power and minimum single-sideband noise figure (SSB NF), including on-chip antenna and duplexer losses, of 6.2 dBm and 20.2 dB, respectively. A system demonstration including a detachable 3-D printed planar lens is also described in Section IV and shows accurate TX/RX beam alignment. The article is concluded in Section V with a comparison with other state-of-the-art sub-THz monostatic radars.

II. Operation Principles and System Architecture

A. Inherent-Loss-Free Full Duplexing

In an FMCW radar, commonly adopted time and frequency duplexing schemes are not feasible. Our work, instead, utilizes wave polarization for in-band full duplexing. As shown in Fig. 2(a), a turnstile antenna with quadrature phase feed generates a right-handed circularly polarized (RHCP) wave radiation; and when the wave reaches an object and gets reflected back, it becomes left-handed circularly polarized (LHCP). In that case, the handedness of the CP waves carries the intrinsic difference between the TX and RX waves.

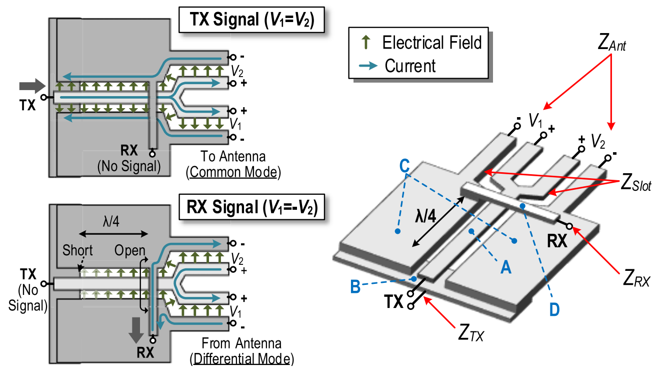

(a)

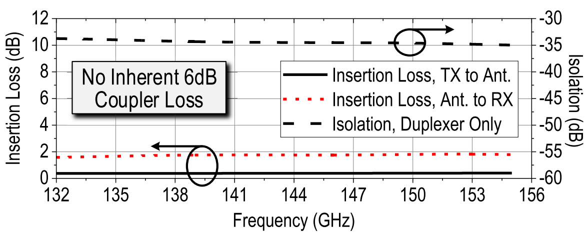

(b)

Fig. 3. Principle of a low-inherent-loss dual-slot duplexer. (a) Duplexer geometry. (b) Simulated performance of the duplexer.

To translate this information into separable circuit signals, the turnstile antenna is driven by two feed ports V_1 and V_2 [see Fig. 2(a)]. With a 90° delay line in the V_2 path, a common-mode excitation (i.e., $V_1 = V_2$) creates an RHCP radiation in the TX mode. Then, a key observation regarding the reflected LHCP wave is while the direction of its propagation is reversed, the direction of the rotation of its electrical field remains the same. As a result, the received RX wave excites signals with the same relative phases among the four antenna branches as in the TX mode. Interestingly, as shown in Fig. 2(b), with the additional 90° delay in the V_2 path, the RX signal at the V_1 and V_2 ports is now in differential mode (i.e., $V_1 = -V_2$).

Next, to redirect these two mode components to corresponding TX and RX circuits, a compact, dual-slot-based duplexer structure is adopted [see Fig. 3(a)], where two identical slots connecting to the V_1 and V_2 ports are placed in parallel, with one shared metal trace (A) in between. The TX port is formed between this metal trace and a metal bridge (B) that connects the two sidewalls (C) of the slots at the left end. Meanwhile, at the right end of the duplexer, the two sidewalls along with a short metal overhang (D) also form the RX port. As a result, those two slots present themselves to be in shunt to the TX port and in series to the RX port. The electrical length between the TX and RX ports is set to be a quarter wavelength ($\lambda/4$). As Fig. 3(a) shows, signal injection at the TX port leads to $V_1 = V_2$ (required for the RHCP TX wave), and the coplanar-waveguide-like (CPW-like) field distribution in the two slots ideally gives equal potential between the two slot sidewalls, hence zero leakage to the RX port (or perfect TX-to-RX isolation). Next, in the RX mode when the LHCP wave creates $V_1 = -V_2$, the electrical potentials in the two slots are summed and extracted at the RX port, but are shorted at the TX port by the metal bridge (B). Through the $\lambda/4$ slots, such a short is then transformed to an open to the RX port, so that the RX signal is entirely diverted from the TX port (or perfect ANT-to-TX isolation).

In summary, this duplexer mitigates any inherent insertion loss, which is not avoidable in prior duplexing coupler designs, if TX, RX, and ANT ports are matched. To realize such matching, the impedances marked in Fig. 3(a) need to satisfy

$$Z_{\text{Slot}}^2 = 2Z_{TX}Z_{\text{Ant}} \tag{2}$$

$$Z_{\text{RX}} = 2Z_{\text{Ant}}. \tag{3}$$

With (2) and (3), the TX port is matched to the common mode of the antenna pair without "seeing" the RX, and the RX port is matched to the differential mode of the antenna pair without "seeing" the TX.

There are three points worth mentioning. First, the adopted circular polarization also mitigates radar clutters caused by the second reflection at the ground, since double reflection turns the wave back to the RHCP mode, which is rejected by the RX. Second, the TX-to-RX isolation of the presented duplexer only relies on geometrical symmetry. The $\lambda/4$ section only affects impedance matching for RX, but it is irrelevant to the TX-to-RX isolation. Therefore, the duplexer should have a broadband frequency response regarding isolation, as is verified by the electromagnetic simulation in Fig. 3(b). The TX-to-RX isolation with matched antenna ports is 34 dB. Such finite isolation is due to the overhang of the RX port, which slightly breaks the structural symmetry. The simulated TX-to-ANT and ANT-to-RX insertion losses, mainly due to metal resistivity, are only 0.4 and 1.6 dB, respectively. Third, the TX-to-RX isolation protected by the geometrical symmetry remains high even at large oblique angles of sensing, where the wave degenerates to linear polarization. As presented in Appendix A and the corresponding results in Fig. 4(b), there is only a maximum 3 dB more inherent ANT-RX insertion loss for 90° oblique angle and near-complete linear polarization. In this work, the radiation to/from the pairing lens is mostly concentrated within $\sim\pm 45°$ oblique angle range, and the simulated, broadside antenna axial ratio including the degradation from the duplexer structure is below 3 dB within 20-GHz bandwidth [see Fig. 4(c)]. As such, the insertion loss increase is expected to be below 1 dB.

B. Isolation Degradation by Antenna Mismatch

Similar to other in-band full-duplex transceivers, antenna mismatch that is unavoidable in broadband operation causes extra TX-to-RX leakage. The effect of internal reflection at the antenna interface is equivalent to having an object in close proximity at the front of the radar. Fig. 5(a) shows an analytical approach to model the leakage caused by antenna mismatch. When a common mode excitation is fed into the antenna, at the right side of Fig. 5(a), the active reflection coefficients Γ_1 and Γ_2 are

$$\Gamma_1 = s_{11} - js_{12} \quad \text{and} \quad \Gamma_2 = s_{22} + js_{21} \tag{4}$$

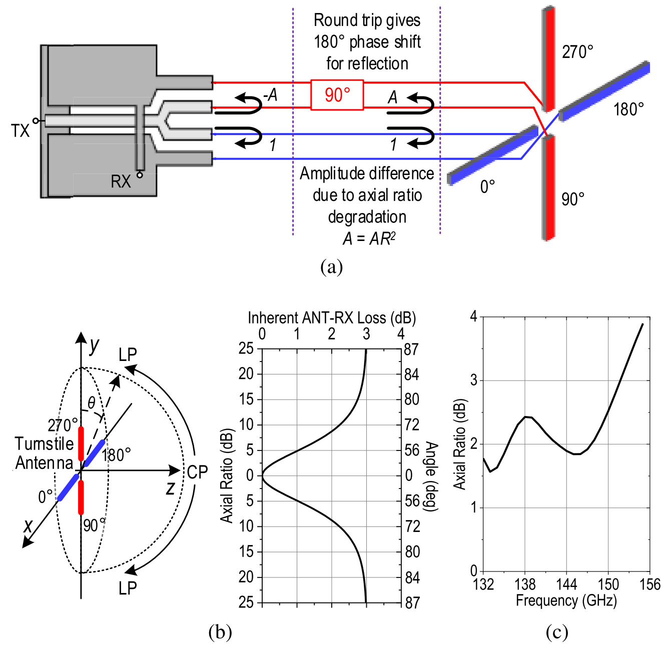

Fig. 4. Axial ratio issue in the CP antenna: (a) axial ratio to amplitude imbalance, (b) calculated extra insertion loss [based on (18)] at various oblique angles and axial ratios, and (c) simulated axial ratio of our antenna (see Section III-A).

respectively, where s_{ij} $(i, j = 1,2)$ is the element of two-port scattering-parameter matrix of the turnstile antenna. Due to the reciprocity and symmetry of the turnstile antenna, one should further have

$$s_{12} = s_{21}, \qquad s_{11} = s_{22}. \tag{5}$$

Now consider the reflected wave toward the TX and RX ports, the round trip through the 90° phase shifting leads to a total of 180° phase difference, and hence turns Γ_1 to $-\Gamma_1$ when it comes to the duplexer interface [the left side of Fig. 5(a)]. Then, from the aforementioned mode analysis, the TX return loss $S_{\mathrm{TT},0}$ and TX-to-RX isolation $S_{RT,0}$ are

$$S_{\mathrm{TT},0} = \frac{-\Gamma_1 + \Gamma_2}{2} = js_{21} \tag{6}$$

$$S_{\mathrm{RT},0} = \frac{\Gamma_2 - (-\Gamma_1)}{2} = s_{11}. \tag{7}$$

Here, the subscript "0" denotes the original isolation level (and return loss) due to antenna mismatch. Later on, an additional technique will be applied to improve it. The intriguing part of (6) and (7) is that, the matching of antenna (s_{11}) contributes to the TX-to-RX isolation, while the crosstalk between two antenna polarizations (s_{21}) contributes to the TX return loss.

C. Adaptive Self-Interference Cancellation (SIC)

To avoid saturation of the receiver, additional efforts are needed to compensate for the antenna mismatch and to improve the TX-to-RX isolation. A key observation from Fig. 5(a) is that antenna mismatch causes imbalanced reflections in the two slots of the duplexer, and it is such an imbalance that induces differential-mode power flow into the RX port. As such, if certain additional imbalanced reflection is

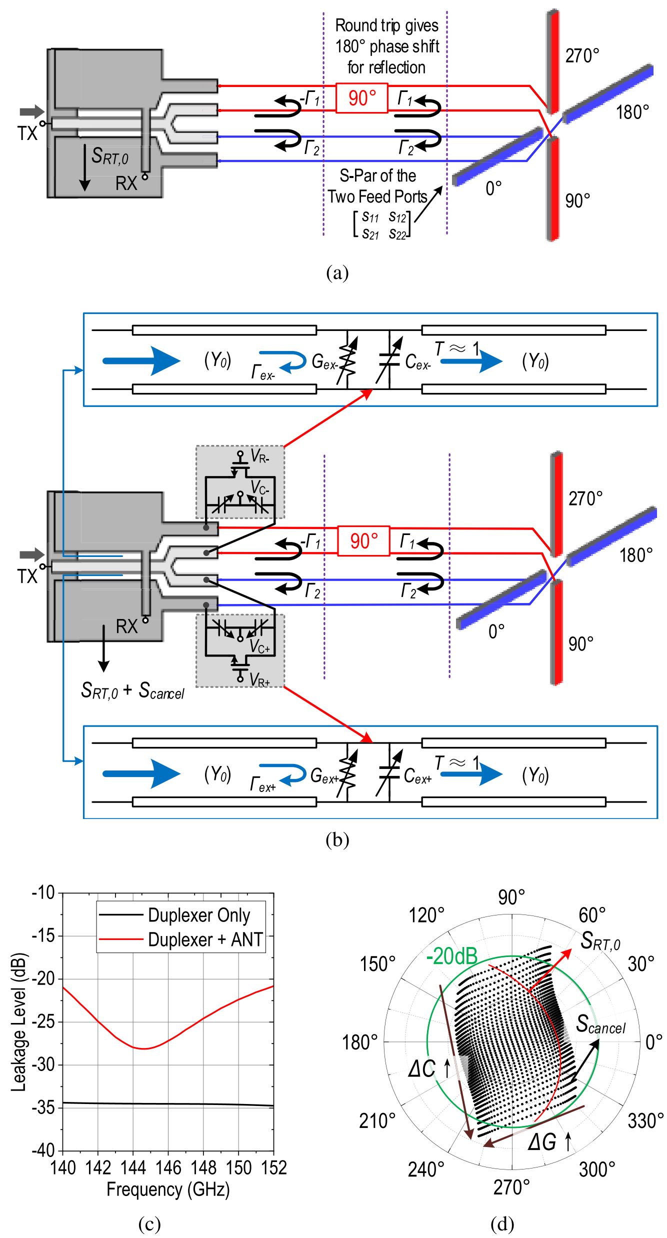

Fig. 5. Analysis of TX-to-RX leakage due to antenna mismatch. (a) Original leakage from antenna reflection. (b) SIC with additional tunable devices and equivalent circuits. (c) Simulated TX-to-RX leakage level. (d) Simulated SIC tuning range.

intentionally created at the same interface, so that it precisely cancels out the original reflection from the antenna, then the overall leakage at the RX port is minimized.

To do that, two sets of transistors and MOS varactors are inserted into the duplexer slots, as shown in Fig. 5(b). These additional devices can be modeled as tunable resistors and capacitors, and together with the transmission line model for each slot, it can be derived that the extra reflection generated by these devices in each slot is

$$\Gamma_{\mathrm{ex}} = -\frac{G + j\omega C}{2Y_0 + G + j\omega C}. \tag{8}$$

Such $\Gamma_{\rm ex}$ in both slots (i.e., $\Gamma_{\rm ex+}$ and $\Gamma_{\rm ex-}$) can be directly added to the original antenna reflections $-\Gamma_1$ and Γ_2, if the condition $|\Gamma_{\rm ex}| \ll 1$ is assumed. Such a condition means that $\Gamma_{\rm ex}$ is a small perturbation to the duplexer and the wave transmission through the added devices has nearly no loss. It is readily satisfied, because the original TX-to-RX leakage is small anyway when the antenna is reasonably well matched (hence only small compensation is required).

Suppose $|\Gamma_{\rm ex}| \ll 1$, then in (8), $|G + j\omega C|$ must be much smaller than $2Y_0$, so that (8) approximates to

$$\Gamma_{\rm ex} \approx -\frac{G + j\omega C}{2Y_0}. \tag{9}$$

At the RX port where the differential mode is extracted, the TX-to-RX isolation after adding the above tunable devices becomes

$$S_{\rm RT} = S_{\rm RT,0} + S_{\rm cancel} \approx S_{\rm RT,0} + \frac{\Gamma_{\rm ex+} - \Gamma_{\rm ex-}}{2}. \tag{10}$$

By substituting (7) and (9) into (10), we further get

$$S_{\rm RT} \approx s_{11} - \frac{\Delta G + j\omega \Delta C}{4Y_0} \tag{11}$$

where $\Delta G = G_{\rm ex+} - G_{\rm ex-}$ and $\Delta C = C_{\rm ex+} - C_{\rm ex-}$ are the device conductance and capacitance differences in the two slots. With a similar process, one can also get the new TX return loss as

$$S_{\rm TT} \approx S_{\rm TT,0} + \frac{\Gamma_{\rm ex+} + \Gamma_{\rm ex-}}{2} = js_{21} - \frac{\bar{G} + j\omega \bar{C}}{2Y_0} \tag{12}$$

where $\bar{G} = (G_{\rm ex+} + G_{\rm ex-})/2$ and $\bar{C} = (C_{\rm ex+} + C_{\rm ex-})/2$ are the average device conductance and capacitance in the two slots. Note that these added tunable devices essentially introduce a tradeoff between the TX return loss and TX-to-RX isolation. A larger $\Delta G + j\omega \Delta C$ in (11) is able to compensate for a larger nonideal antenna mismatch (i.e., s_{11}), but that comes with the cost of a worse $|S_{\rm TT}|$, because $\bar{G} + j\omega \bar{C}$ in (12) is likely to be larger as well since no negative G or C is possible in this scenario.[2]

In order to size the tunable devices, the actual antenna mismatch (equivalent to the isolation/leakage; recall from Section II-B) is simulated in Fig. 5(c), while the antenna details are discussed in Section III-A. According to (11), device tuning ranges ΔG and ΔC limit the leakage cancellation ability. As illustrated in Fig. 5(d), after carefully considering the tradeoffs between TX return loss and TX-to-RX isolation, the original leakage from 140 to 152 GHz is fully covered by the device impedance tuning range in the polar plot, so that effective leakage cancellation is applied at every frequency point within the bandwidth. In practice, because of the parasitics of devices, the actual device tuning range on the polar plot is distorted from a perfect rectangular shape with respect to the real and imaginary axes, as plotted in Fig. 5(d).

Furthermore, as illustrated in Fig. 6, the dispersive character of antenna reflection makes the corresponding group delay

[2]A larger ΔG between the two slots means a larger $\bar{G}$, once the smaller G in one of the slots diminishes to zero. The same applies to C.

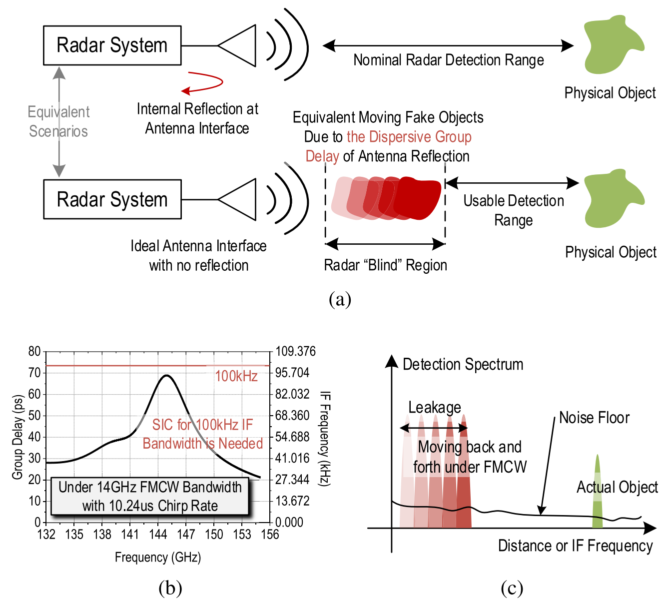

Fig. 6. Antenna mismatch issues: (a) leakage caused by internal reflection at the antenna interface, (b) simulated group delay of antenna reflection, and (c) theoretical IF spectrum with leakage.

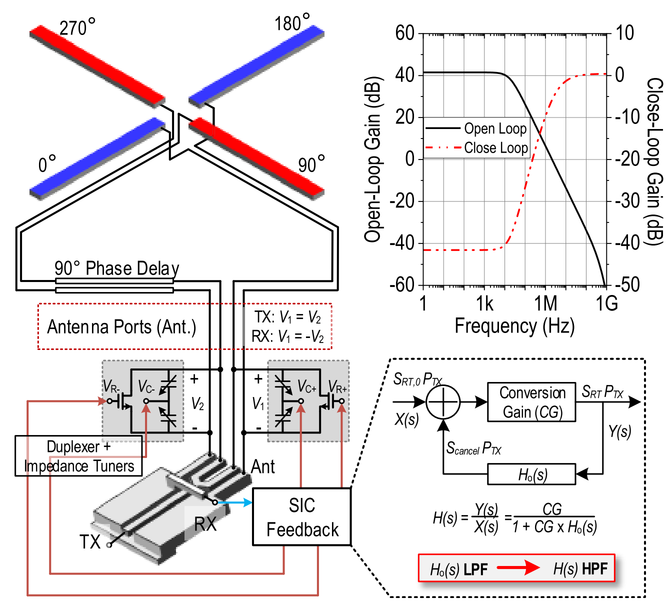

Fig. 7. Adaptive SIC feedback loop with the antenna and duplexer. A closed-loop small-signal transfer function is equivalent to an active HPF.

time vary at different frequencies [20–70 ps between 132–156 GHz in our simulation in Fig. 6(b)]. Since this group delay time is equivalent to the time of flight for that "fake object," the dynamic feature mimics its movement. Thus, when a wide-band signal (e.g., FMCW chirp) is applied, this dispersive antenna mismatch dynamically changes the instantaneous leakage level.

This dispersion of antenna mismatch, therefore, requires a dynamic SIC. For different frequencies in an FMCW chirp, the original TX-to-RX leakage at the antenna interface varies and the bias voltages of the SIC tunable devices must change

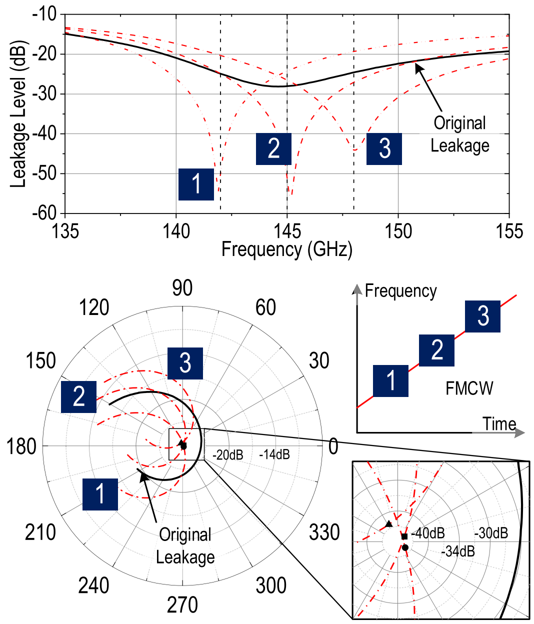

Fig. 8. Behavioral simulation of the closed-loop response for the SIC feedback.

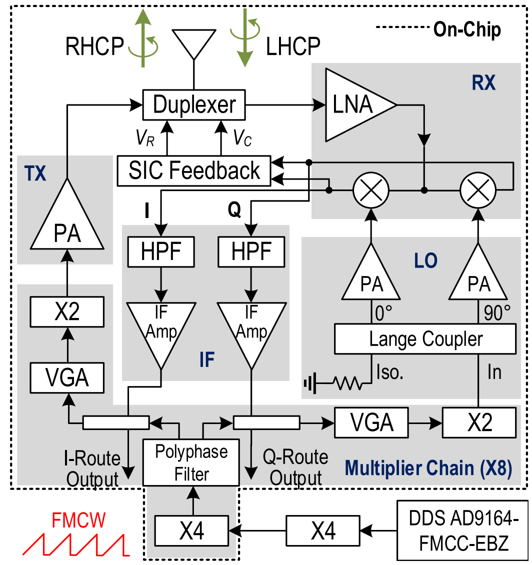

Fig. 9. System architecture of the monostatic radar transceiver chip.

according to (11). A lookup table-based approach is not desired, because the calibration of each individual chip is needed, and PVT variation may render the SIC less effective over time. In order to automate the dynamic SIC, a feedback control loop similar to that in [25] is adopted, in which the tunable device bias voltages are generated from low-pass-filtered (LPF) RX baseband I/Q signals serving as indicators for the leakage amplitude and phase (see Fig. 7). A variable-gain-amplifier-based (VGA-based) phase tuner is applied to arbitrarily control the sign and phase of the I/Q signals. A second-stage baseband amplifier generates an open-loop gain of feedback that is large for a low-IF leakage signal and small for the high-IF radar echo signals. Note that a one-time sign control and phase tuning are needed to ensure the negative feedback operation, so that the dynamic leakage is always effectively canceled along the shortest path on the polar plot in Fig. 5(d) and the whole loop never self-oscillates. Details of the SIC circuits are given in Section III-D.

As explained in Fig. 7, after closing the feedback loop, the adaptive closed-loop response is equivalent to an active high-pass filter (HPF), which suppresses the sub-THz leakage that causes the low-frequency IF output. Such adaptive SIC is then able to prevent LNA saturation. It is noteworthy that accurate numerical simulation of this SIC feedback is difficult, since it requires an antenna and nonlinear circuit simulations from sub-THz all the way down to MHz IF frequencies. Therefore, a system-level behavioral simulation is performed using MATLAB by treating the sub-THz receiver chain (excluding the antenna) as a nondispersive linear transfer function. The results are shown in Fig. 8: the isolation curve tracks the sweeping during the FMCW chirp, and leakage suppression always occurs at the instantaneous frequency. This is also manifested in the polar plot in Fig. 8: the adaptive SIC is actually "moving" the whole antenna reflection curve around the complex plane, so that the point on the curve corresponding to the instantaneous frequency remains close to the origin.

D. System Architecture

Fig. 9 shows the system architecture of the presented transceiver chip. Two $\times 8$ multiplier chains are used to turn an input at $\sim$17.5 GHz to the TX and LO signals at $\sim$140 GHz. In both the TX and LO paths, 4-stage, two-way power amplifiers (PAs) are adopted. The TX, ANT, and RX signals are circulated by the full-duplexer presented in Section II-A. The RX chain includes a two-stage low-noise amplifier (LNA), and the output of the LNA is connected to two mixers for I/Q downconversion. The I/Q IF signals are then fed into both the SIC feedback loop and the outputs of the chip. In the I/Q IF paths, HPFs are inserted before the IF amplifiers for further suppression of the leakage at the IF outputs.

III. Circuit Implementations

A. Integrated Hollow Turnstile Antenna Design

The on-chip turnstile antenna in this work, shown in Fig. 10(a), is based on a crossed hollow bow-tie design, with a PCB metal reflector behind the silicon substrate. Due to the high dielectric constant of silicon, most of the radiated wave goes into silicon first and is then reflected back from the PCB reflector, leading to frontside radiation. The substrate thickness is chosen to be 150 μm, or about a quarter wavelength at 140 GHz in silicon, so that the reflected wave is added in phase with the original frontside radiation to the air. Next, we describe the design details of the antenna to simultaneously achieve the following goals: 1) broadband matching for improved TX-to-RX isolation and relaxed SIC requirement; 2) maximum radiation efficiency for enhanced radar operational range; and 3) a low axial ratio of circular polarization for efficient full duplexing described in Section II.

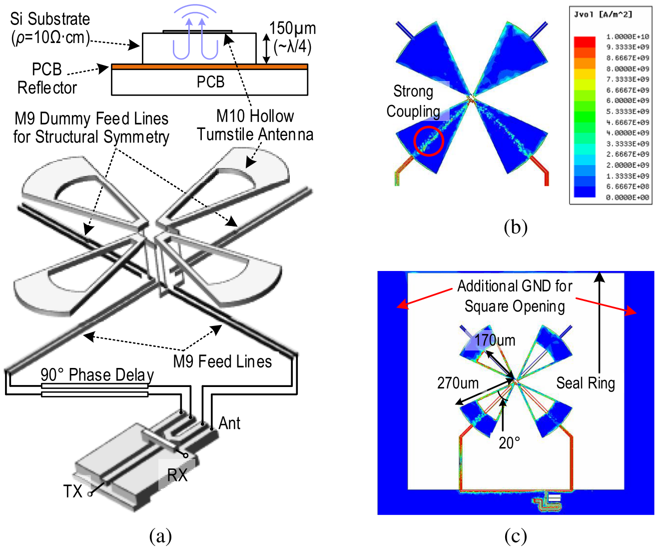

Fig. 10. Integrated hollow turnstile antenna design: (a) antenna geometry with duplexer connection, (b) current distribution of the traditional turnstile antenna, and (c) current distribution of the hollow turnstile antenna; square opening with additional solid GND aside.

The cross bow-ties are chosen for their high inherent bandwidth compared to normal dipoles. Two step lines [see Fig. 10(a)] are then adopted for the impedance matching to the duplexer slots. It is noteworthy that the simulated current distribution in Fig. 10(b) shows a strong coupling between the antenna layer and the feedlines. Such coupling disturbs the antenna resonance and degrades both the radiation efficiency and axial ratio. Interestingly, we also observe from Fig. 10(b) that, most currents contributing to radiation are gathered only on the edges of each fan of the bow-tie, whereas the undesired coupling happens mainly in the middle of the fan. Such a phenomenon is utilized in our design: the middle of each fan is made to be hollow [see Fig. 10(c)], so that the coupling with feedlines is significantly reduced without much disturbance of the desired radiation currents. Moreover, the hollow antenna fans also have less blockage of the reflected wave from the PCB reflector, which improves the radiation efficiency. As plotted in Fig. 11(a), the hollow shape alone improves the radiation efficiency from 20% to 32%. Note that the simulated radiation efficiency plotted in Fig. 11(a) includes the duplexer loss.

The geometrical symmetry of the antenna plus its feedlines is critical to keeping the axial ratio low. In [29], that is achieved with four identical feedlines on the four quads of the circularly polarized antennas. Our work [see Fig. 10(a)], in comparison, adopts a dual-feed scheme for the compactness of the duplexer structure. To keep the geometrical symmetry of the antenna, two dummy feedlines without an electrical connection to the antenna are added. The ground opening around the antenna also has a square shape [see Fig. 10(c)], in order to keep structural symmetry and the circular polarization of the radiation. The simulation in Fig. 11(b) shows that these efforts, along with the hollow antenna shape, reduce the axial ratio to below 3 dB.

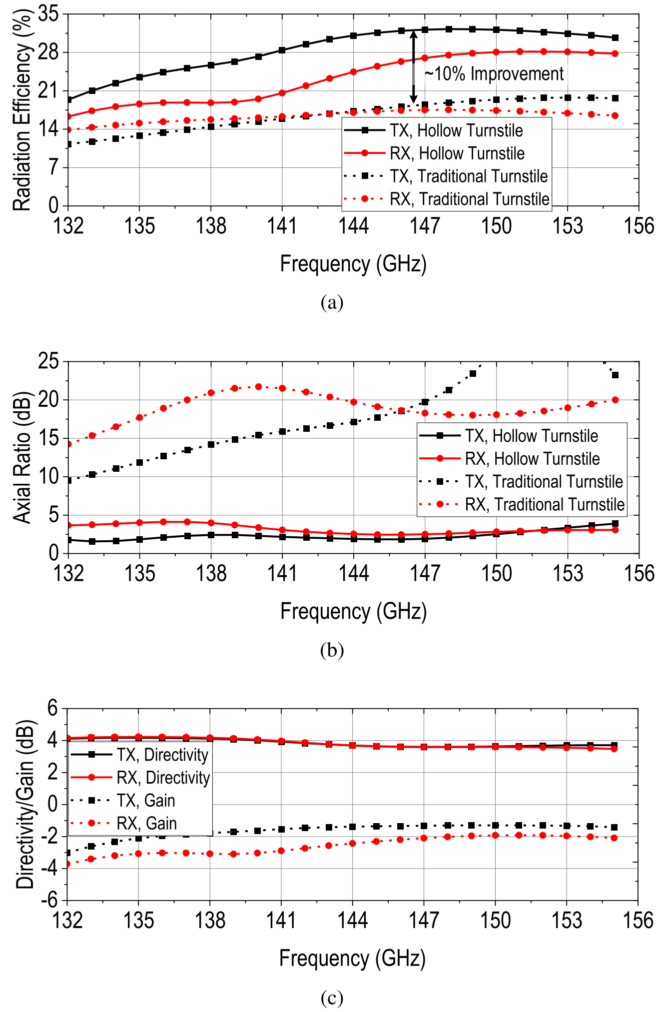

Fig. 11. Simulated results of antenna design (duplexer loss included): (a) radiation efficiency, (b) axial ratio, and (c) antenna directivity and gain.

Fig. 11(c) shows the simulated antenna directivity and gain under TX and RX cases. The single shared antenna topology caused nearly the same directivity number for TX and RX. Nevertheless, the difference in antenna gains between TX and RX indicates slightly higher duplexer loss in the RX case, which is due to the extra radiation loss from duplexer slots under differential mode operation (RX).

B. Sub-THz Transmitter Chain

The sub-THz transmitter chain contains a four-stage, two-way PA. The schematics of the PA are shown in Fig. 12(a), where each stage has a cross-coupled topology for neutralization. GCPW-slot-based power splitters/combiners are adopted at the input-output of the PA, to generate ultralow-loss power splitting and combining. Compared to the traditional transformer-based combiner commonly used for PAs, the smooth transition from the slot to GCPW in the presented splitters/combiners effectively reduces insertion loss and increases PA output power. Detailed principles of the structure are discussed in [31]. Fig. 12(b) shows the simulated insertion loss of the power combiner at the PA output. Considering

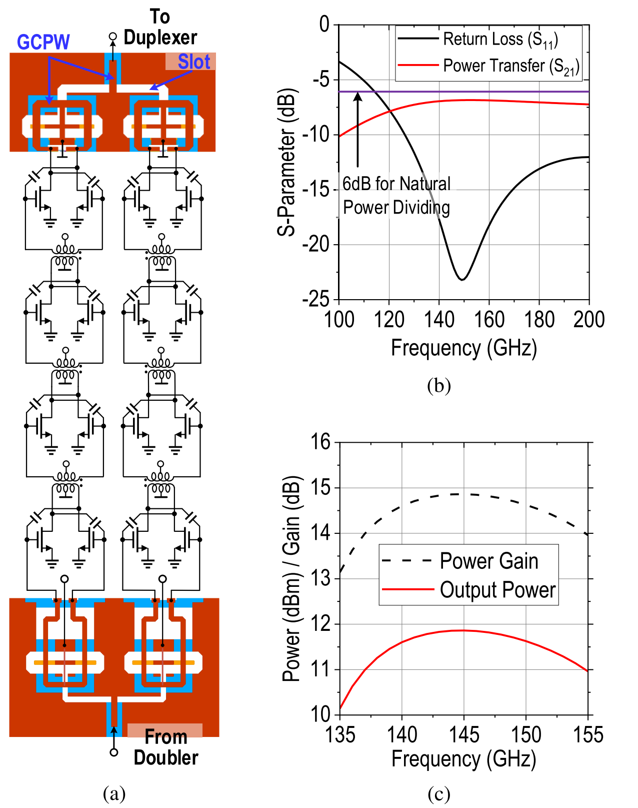

Fig. 12. TX PA design. (a) PA schematics. (b) Return loss and power transfer for the combiner. (c) Simulated PA power gain and output power.

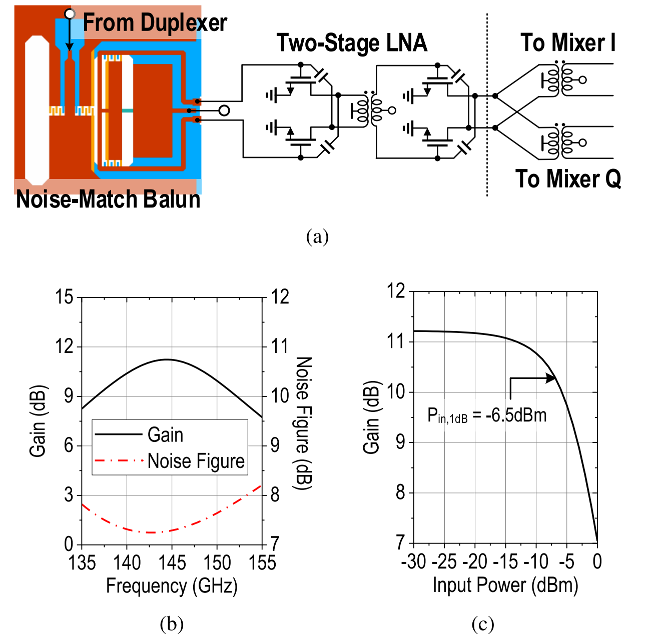

Fig. 13. RX LNA design. (a) LNA schematics. (b) Simulated LNA gain and NF. (c) Simulated LNA 1 dB input compression point.

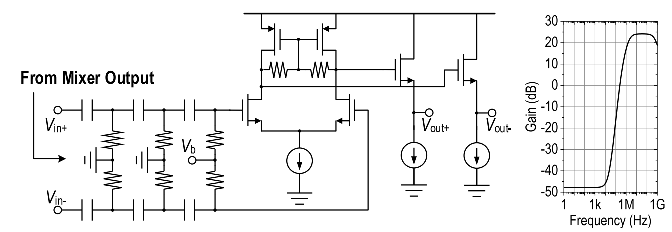

Fig. 14. Schematics and simulated performance of the IF circuits.

that the power splitting ratio is 1:4, the ideal, lossless power transmission of the combiner is −6 dB. Therefore, the actual insertion loss of the combiner is only 0.8 dB. Thanks to such ultralow insertion loss, the PA has a simulated output power over 11 dBm across 18-GHz bandwidth, as shown in Fig. 12(c). The simulated PA gain within that bandwidth is around 15 dB.

C. Sub-THz Receiver Chain

The sub-THz receiver chain starts from a 140-GHz LNA with two cascaded neutralized stages and a noise-matched input balun. The LNA schematics together with the input balun are illustrated in Fig. 13(a), and its simulation results are in Fig. 13(b) and (c). The simulated gain, noise figure (NF), and $P_{\mathrm{in},1\ \mathrm{dB}}$ of the LNA including the input balun are 11 dB, 7.3 dB, and −6.5 dBm, respectively. A tradeoff between the LNA gain and linearity is intentionally applied here, in order to conservatively protect the RX from saturation due to the potential TX-to-RX leakage. The output of the LNA is then connected to two mixers for I-Q downconversion. Passive Gilbert mixer topology is chosen to avoid excessive flicker noise that disturbs the SIC feedback loop and lowers the sensitivity. The simulated SSB NF of the LNA plus mixer chain is below 12 dB across 20-GHz bandwidth. The I/Q LO signals are generated from two identical four-stage, one-way PAs with a topology similar to that of the PAs in TX, except that there are no splitters or combiners. To create the quadrature LO phases, a Lange coupler is added to the inputs of LO PAs. Fig. 14 shows the schematics and simulated performance of the IF circuits implemented at each I/Q path. The mixer outputs go through an HPF first and then an IF amplifier, so that the leakage signal can be further suppressed down at the IF domain.

D. SIC Circuits

The block diagram of SIC circuits is shown in Fig. 15(a), and the open-loop SIC feedback consists of two cascaded stages. The first stage is a VGA-based phase tuner (rotator), and its schematic is shown in Fig. 15(b). The VGA configuration is similar to that in [32], which has a highly linear response to rotating the I/Q signals in the first quadrant. Then by switching signs for the differential inputs of both I and Q routes, a complete 360° rotation can be achieved. The second stage of the SIC feedback is basically two IF amplifiers with off-chip capacitive loads [see Fig. 15(c)], which serve as two active LPFs. The passband of the open-loop SIC circuits is determined by the IF frequency from antenna reflection-induced leakage, which can be calculated by the antenna group delay and applied FMCW chirp rate. As shown in Fig. 6(b), the maximum simulated group delay is below 70 ps, so under the FMCW chirp rate (10.24 μs per chirp) used in measurement,

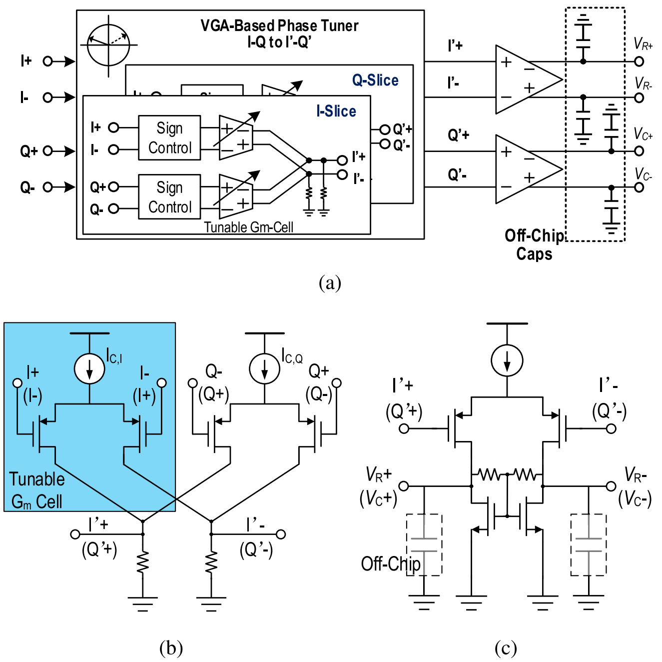

Fig. 15. SIC feedback circuits. (a) Block diagram for open-loop circuits. (b) First stage of open-loop circuits. (c) Second stage of open-loop circuits.

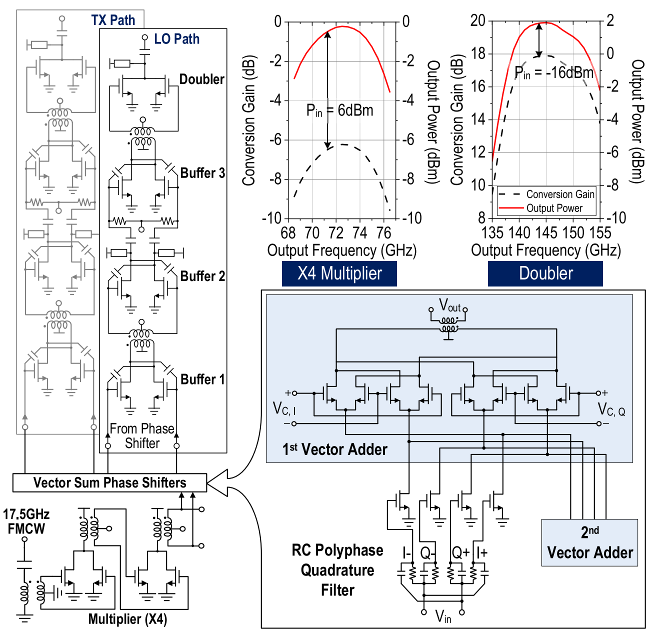

Fig. 16. Schematics of the input multiplier chain. Simulated performance of the ×4 multiplier and doubler.

the corresponding IF frequency for leakage should be below 100 kHz. With tradeoffs on phase margin and roll-off for the open-loop active LPF, the final design of the open-loop SIC circuits shows an overall simulated frequency response as illustrated in Fig. 7.

E. Input Multiplier Chain

An input multiplier chain is implemented to provide both the TX and LO signals. As shown in Fig. 9, the first stage

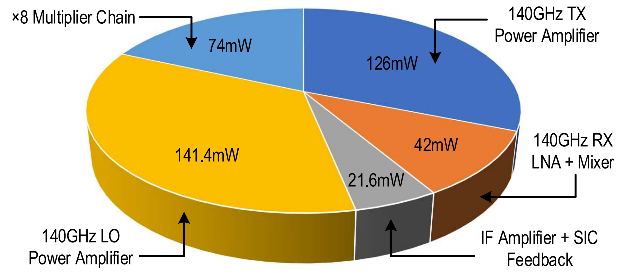

Fig. 17. Measured dc power consumption for different subcircuits.

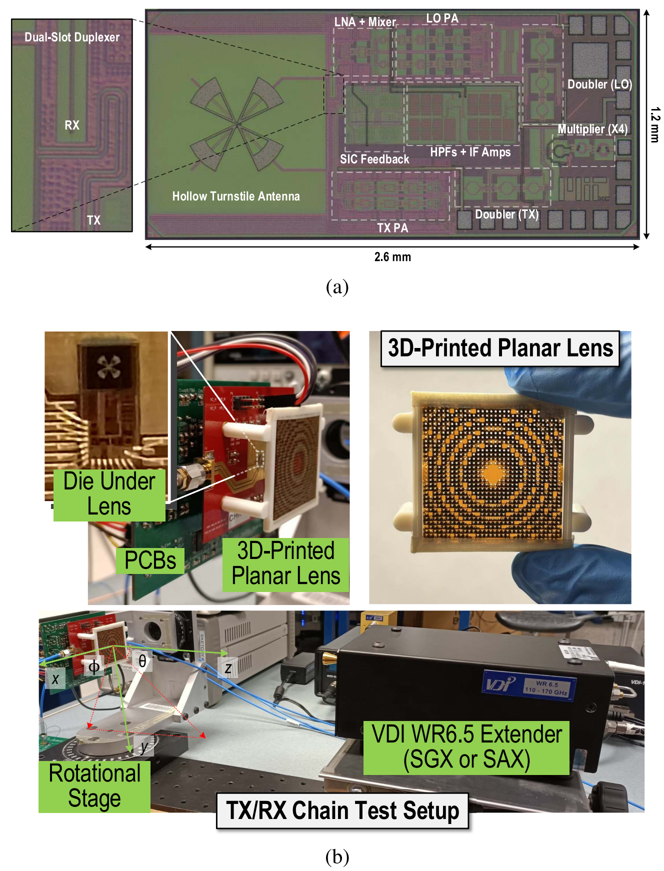

Fig. 18. Photographs of (a) 140-GHz monostatic radar transceiver chip and (b) chip assembly with PCBs and TX/RX chain measurement setups.

of the chain is a 70-GHz, ×4 multiplier, whose schematics are shown in Fig. 16. The 70-GHz signal is then split into two paths for TX and LO through two VGA-based phase shifters, as illustrated in Fig. 16. These phase shifters can adjust the relative phase between TX and LO, which is set to zero for default monostatic operations. Lastly, the 70-GHz signals in both paths are sent to two identical doublers (see Fig. 16) to generate the final 140-GHz signals. The doubler consists of three cascaded buffer stages, in order to improve the conversion efficiency of the last doubler stage.

IV. Measurement Results

The chip is fabricated using a 65-nm bulk CMOS technology, with 3.1 mm^2 of area and 405 mW of measured

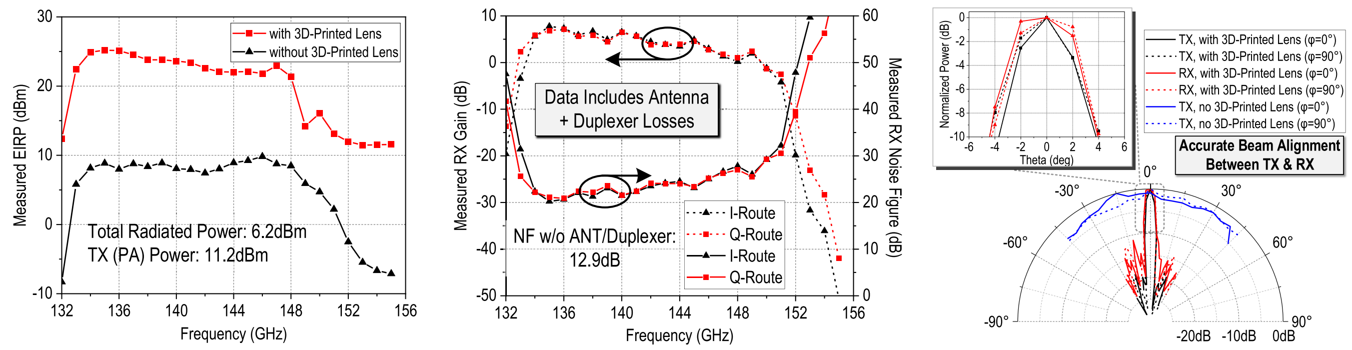

Fig. 19. TX/RX chain measurement results. (a) TX EIRP, total radiated power, and TX (PA) power. (b) RX CG and NF. (c) TX/RX radiation patterns.

power consumption (see Fig. 17). The die micrograph and the system assembly are shown in Fig. 18. The chip is mounted on a PCB with standard wire bonding. Enabled by the monostatic frontside radiation scheme, the chip can pair with a detachable planar lens with 39 × 39 × 1.3 mm^3 size [see Fig. 18(b)]. Realized via 3-D polymer and metal additive printing, the lens has 24 × 24 metasurface resonator units based on metal-grating structures with various dimensions to offer 0°–315° (with 45° step size) local phase shifting [33]. Compared to a standard dielectric lens used in [15], it has an ultralow profile (91.7% lower for the lens itself, and 40.7% lower for the overall height) and offers broadband, ∼15 dB of gain boosting.

A. TX/RX Chain Performances

For TX measurement, the chip input is connected to a signal source (N5173B) without frequency modulation and radiates out 140-GHz power. The chip package is fixed on a rotational stage movable in both azimuth (ϕ) and elevation (θ) angles [see Fig. 18(b)]. The power is then received by a VDI WR-6.5 horn antenna. A VDI Erickson PM5 powermeter is used for accurate measurement of absolute radiated power, and a VDI WR-6.5 spectrum analyzer extender (SAX) driven by an LO source (E8257D) is used to measure the radiation pattern and spectrum [see Fig. 18(b)]. Since the chip radiates a circularly polarized wave while the VDI horn antenna is for linear polarization, chip radiation patterns in both $\phi = 0°$ and $\phi = 90°$ planes are measured, with two orthogonal linear polarizations (x and y polarizations) in each plane, and the total radiated power is calculated by adding the results from both polarizations together. A similar treatment is applied in the RX measurement as well.

In the RX measurement [see Fig. 18(b)], the IF outputs of the chip are connected to a spectrum analyzer (N9020A), and the VDI horn antenna is now used as a radiator driven by a VDI WR-6.5 signal generator extender (SGX). This setup is used to measure the RX conversion gain (CG) and NF. The RX radiation pattern is also measured, in order to check whether accurate TX and RX beam alignment is obtained.

With the calculation from the Friis equation, the measured peak effective isotropic radiated power (EIRP) [see Fig. 19(a)] is 25.2 dBm with the lens and 9.8 dBm without the lens. The measured, lens-enhanced radiation patterns for both TX and RX are shown in Fig. 19(c). Not only a sharp (∼4°) beam profile, but also accurate TX and RX beam alignment are observed, thanks to the monostatic configuration of the chip. Based on the measured radiation directivity and the simulated radiation efficiency without the lens, the total TX radiated power and the PA-generated power are estimated to be 6.2 and 11.2 dBm, respectively. Fig. 19(a) also shows that the chip 3-dB TX bandwidth is 15 GHz (i.e., from 133 to 148 GHz). The measured PA-generated power matches well with the simulation results in Fig. 12(a).

Using the gain method discussed in [15], the measured RX CG and SSB NF are given in Fig. 19(b). The minimum SSB NF, including the antenna and duplexer loss, is 20.2 dB for both I/Q paths. After de-embedding the simulated antenna and duplexer loss, the minimum SSB NF for the receiver circuits only is estimated to be 12.9 dB, which is close to the simulated value of 12 dB.

B. Radar Detection Setups and Results

To perform the actual monostatic radar detection, the setup in Fig. 20 is established. An FMCW chirp signal centered around 4.375 GHz is first generated by an off-chip DDS board (AD9164-FMCC-EBZ) and then sent to the chip input through an off-chip ×4 multiplier chain. The original FMCW signal from the DDS board has a bandwidth of 427.5 MHz and a chirp period of 10.24 μs; so after the off-chip ×4 and on-chip ×8 multiplication, the sub-THz bandwidth of the radar output is 14 GHz, which is within the available hardware bandwidth measured in Fig. 19(a). The I/Q IF outputs of the chip receiving the echoed signal are then sent to an off-chip digitizer (NI-PXI-5105). The IF signal is synchronized with the transmitted FMCW chirps through a global clock between the DDS DAC and the digitizer. The setup hardware is controlled by an Arduino microcontroller board, and the digitized radar signal is further processed in a PC.

The radar ranging measurement results are shown in Fig. 21(a). Since the radar utilizes circularly polarized waves, commonly used corner reflectors cannot be set as test objects because they generate double reflections, hence the same handedness of the circular polarization between TX and RX waves. Instead, a planar metal plate is used as the object

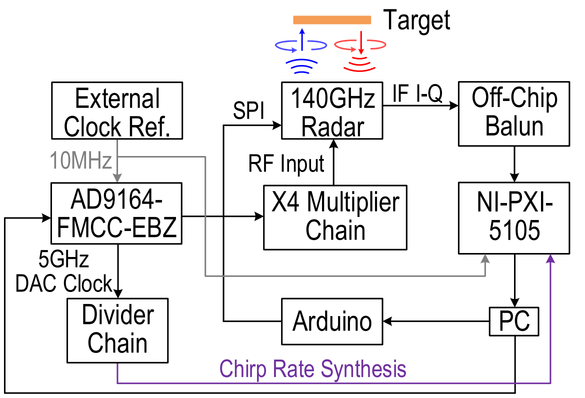

Fig. 20. 140-GHz radar detection setup.

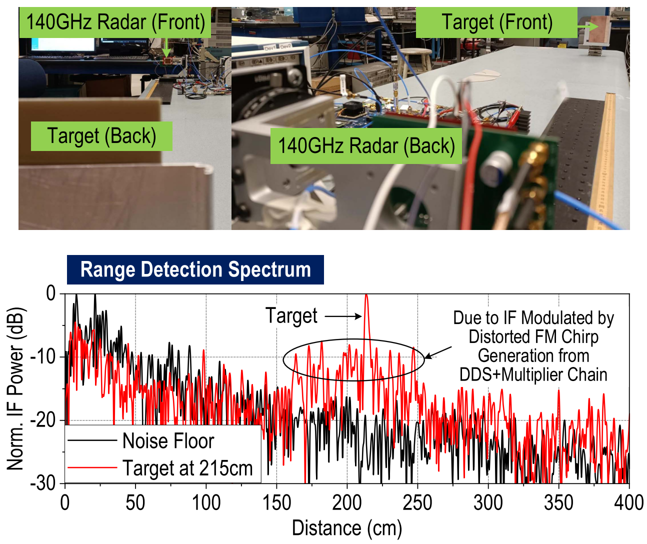

(a)

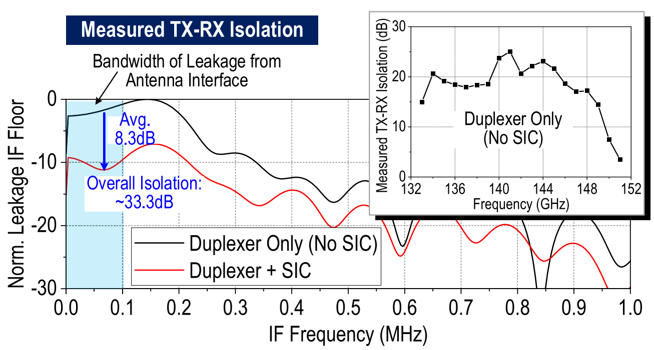

(b)

Fig. 21. Radar detection demonstration: (a) range detection and (b) measured TX-to-RX isolation performance.

for the presented radar detection. In Fig. 21(a), the metal plate is placed in front of the radar, and after background scattering calibration and basic signal processing (e.g., Fourier transform), a clear detection peak is observed on the detection spectrum. The corresponding detected target location (distance = 215 cm) agrees well with the actual physical distance between the metal plate and the radar. Note that the spurious

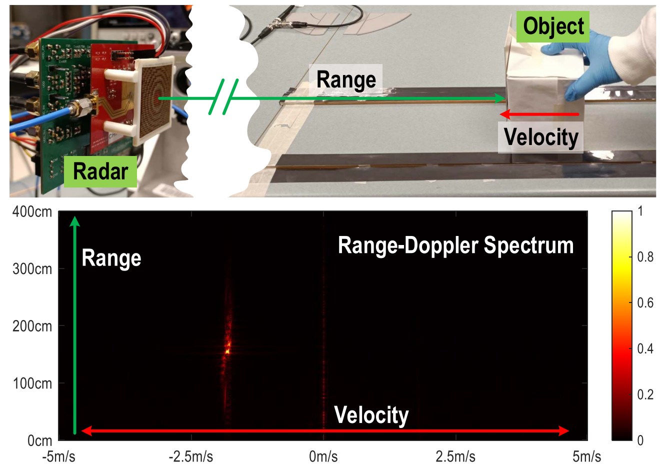

Fig. 22. Radar range-Doppler detection demonstration.

tones close to the target peak and ~10 dB lower in power are due to nonlinear distortion of the generated FMCW signal from the DDS board and the off-chip multiplier chain.

With the same setup, the TX-to-RX isolation performance is also measured by comparing the IF signal spectrum with and without the SIC feedback loop closed. As demonstrated in Fig. 21(b), under a 14-GHz FMCW chirp modulation, excessive IF components below 100 kHz are observed, which corresponds to the TX-to-RX leakage and the simulated antenna group delay (see Fig. 6), as discussed in Section II. When the SIC feedback loop is closed, such low-frequency components are decreased by 8.3 dB on average, which shows the effectiveness of the SIC loop. The inset in Fig. 21(b) also shows the original isolation level without SIC over the operation frequency range, which is acquired by feeding the chip with a single-tone signal and measuring the corresponding dc voltages (due to homodyne mixing between the TX-to-RX leakage and the RX LO) at both I/Q IF outputs. Such isolation is solely provided by the electromagnetic wave mode duplexing. That, along with the additional SIC suppression, leads to overall isolation of ~33.3 dB for the system under the 14-GHz FMCW chirping.

When the metal plate moves along the longitudinal direction in front of the radar, Doppler effects occur. By performing one more dimension of Fourier transform, a 2-D range-Doppler spectrum [34] is obtained in Fig. 22, corresponding to both the target position and its velocity.

V. CONCLUSION

In-band TX/RX-antenna-sharing generally implies the breaking of reciprocity. For on-chip systems, due to the lack of nonmagnetic components, nonreciprocity requires either: 1) time-varying or nonlinear components or 2) passive four-port networks such as directional/hybrid couplers. However, the former is not suitable for high-frequency operations, and the latter has 3 dB + 3 dB inherent loss. This article shows that, in the case of radar sensing, the above seemingly fundamental dilemma can be well addressed: monostatic operation is realized through a fully passive antenna and duplexer structures

TABLE I
PERFORMANCE COMPARISON WITH OTHER STATE-OF-THE-ART INTEGRATED MONOSTATIC RADARS

References	**This Work**	JSSC 2021 [26]	T-THz 2016 [29]	T-MTT 2017 [4]	ISSCC 2020 [25]	T-MTT 2018 [28]
Technology	65-nm CMOS	130-nm SiGe	130-nm SiGe	130-nm CMOS	65-nm CMOS	130-nm SiGe
Frequency (GHz)	134∼148	160∼178	210∼270	23.8∼24.5	80∼85	150∼170
Inherent 6 dB Coupler Loss?	No	Yes	No	Yes	Yes	Yes
EIRP (dBm)	9.8, 25.2[(a)]	8	32.8[(e)]	N/A	17[(g)]	32[(i)]
TX Power (dBm)	11.2[(b)]	3	N/A	-1.6	2	3
Total Radiated Power (dBm)	6.2	N/A	5	N/A	N/A	N/A
RX $\mathrm{NF_{min}}$ (dB)	12.9	15.5	∼19	11.6	15	20
Adaptive SIC	Yes	No	No	No	Yes	No
Isolation (dB)	33.3[(c)]	25	26	47.3[(f)]	40[(h)]	17
Antenna Type	On-Chip	On-Chip	On-Chip	Off-Chip	Off-Chip	Off-Chip
Radiation Direction & Antenna Feature	Front-Side with 3D-Printed Planar Lens	Back-Side with Substrate Etching[(d)]	Back-Side with Silicon Lens	Horn Antenna	4×8 Patch Antenna Array	Dielectric Resonator Antenna
Die Area ($\mathrm{mm^2}$)	3.1	5.4	3.2	1.5	1	1.9
DC Power (mW)	405	860	1600∼2000	111	120	N/A

[(a)] with 3D-printed lens [(b)] assuming 32% simulated antenna efficiency [(c)] under 14-GHz-wide FMCW chirping [(d)] localized backside etching
[(e)] with silicon lens [(f)] achieved in a narrow-band by manual impedance tuning [(g)] with off-chip 4×8 patch antenna array
[(h)] reported in a narrow-band measurement [(i)] with off-chip dielectric-resonator antenna

without inherent loss. It is important to clarify that such an advance does not imply that the above theory of reciprocity fails to hold. That is because the TX and RX signals through the ANT port differ in their electromagnetic modes, and our duplexing interface is still reciprocal. It is also noteworthy that in our design, the TX-to-RX isolation—the most critical and challenging metric in full duplex systems—is protected by the geometrical symmetry of on-chip passives, which holds over a wide frequency range with no inherent power waste penalty. Although the mismatch of the ANT port degrades the isolation, that is partially compensated by our adaptive SIC technique.

Table I summarizes the comparison between this work and other state-of-the-art integrated monostatic radars. Compared to other works, the presented chip achieves the highest total radiated power and is the only one that has a >30 dB TX-to-RX isolation level while mitigating the 6-dB inherent coupler loss. Even higher isolation was achieved by other works but with specific limitations: the 47.3 dB isolation level achieved in [4] requires manual impedance tuning of the duplexer and is in a narrow, 0.7-GHz bandwidth with a lower center frequency of 24 GHz. The 40 dB isolation level in [25] is only reported in a narrow-band measurement, although its system bandwidth is 5 GHz. Thanks to the frontside radiation scheme, our system can be paired with a detachable 3-D printed planar lens, which not only boosts the directivity at a low cost, but also develops the great potential for further beam manipulation, such as electrical beam steering using large-scale reflect/transmit arrays.

APPENDIX A
DUPLEXER LOSS RELATED TO ANTENNA AXIAL RATIO

The circular polarization of the turnstile antenna relies on the two orthogonal linear polarizations with equal amplitude. However, the radiation strength of one bow-tie (or dipole) antenna varies significantly at large oblique angles. As shown in Fig. 4(a), in the y–z plane, when the elevation angle θ goes to 0° or 180°, the red dipole reaches the null of its radiation pattern, while the blue one still maintains strong radiation. Therefore, the overall polarization at that angle becomes almost linear, or the axial ratio AR approaches infinity. As the simulation in Fig. 4(b) shows, AR increases to 3 dB at $\theta = 30°$ and 6 dB at $\theta = 60°$.

Such axial ratio degradation is translated to imbalanced amplitudes of RX signals in the two slot lines of the duplexer in Fig. 4(a). Without loss of generality, we assume that the radiation of the bow-tie connecting to the blue route in Fig. 4(a) has a larger degradation at a certain angle, correspondingly normalizes the RX voltage in the blue route, and denotes the RX voltage in the red route as $-A$, where $A \geq 1$ is a real number. The above minus sign represents the round trip 180° phase shift in the red route, as explained in Section II. Based on reciprocity, A is doubly affected by the degradation of axial ratio AR in both the TX and RX processes, so according to the definition of AR ($AR > 1$), A can be expressed as

$$A = AR^2. \tag{13}$$

The differential voltage received by the RX port of the duplexer is then

$$V_{\mathrm{RX}} = 1 - (-A) = 1 + A. \tag{14}$$

Recall from (3), the RX port impedance Z_{RX} is twice the antenna impedance Z_{Ant}, so the RX received power is

$$P_{\mathrm{RX}} = \frac{(1+A)^2}{2Z_{\mathrm{RX}}} = \frac{(1+A)^2}{4Z_{\mathrm{Ant}}}. \tag{15}$$

In comparison, the total power received from the two bow-ties is

$$P_{\text{tot}} = \frac{1^2}{2Z_{\text{Ant}}} + \frac{A^2}{2Z_{\text{Ant}}} = \frac{1+A^2}{2Z_{\text{Ant}}}. \tag{16}$$

Thus, the overall TX→ANT→RX power efficiency, compared to a radar using only linearly polarized waves, is

$$\eta = \frac{P_{\text{RX}}}{P_{\text{tot}}} = \frac{(1+A)^2}{2\left(1+A^2\right)} = \frac{\left(1+\text{AR}^2\right)^2}{2\left(1+\text{AR}^4\right)}. \tag{17}$$

From Cauchy–Schwarz inequality, we have $\eta \leq 1$. The overall duplex insertion loss, in dB, is then

$$L = 10\log_{10}\left(\frac{1}{\eta}\right) = 10\log_{10}\frac{2\left(1+\text{AR}^4\right)}{\left(1+\text{AR}^2\right)^2}. \tag{18}$$

When AR $=1$ (circular polarization), we have $\eta = 1$ and $L = 0$ dB. Interestingly, even in the worst scenario when AR is infinity (linear polarization), we still have $\eta = 0.5$ or $L =$ 3 dB, which is 3 dB better than directional/hybrid coupler-based duplex solutions.

Plotting (18) in dB scale gives the curve as shown in Fig. 4(b).

Acknowledgment

The authors would like to thank Virginia Diodes Inc. (VDI), Charlottesville, VA, USA, for the support of test instruments.

References

[1] C. Li and J. Lin, "Random body movement cancellation in Doppler radar vital sign detection," *IEEE Trans. Microw. Theory Techn.*, vol. 56, no. 12, pp. 3143–3152, Dec. 2008.

[2] J. Hasch, E. Topak, R. Schnabel, T. Zwick, R. Weigel, and C. Waldschmidt, "Millimeter-wave technology for automotive radar sensors in the 77 GHz frequency band," *IEEE Trans. Microw. Theory Techn.*, vol. 60, no. 3, pp. 845–860, Sep. 2012.

[3] W. Menzel, "Millimeter-wave radar for civil applications," in *Proc. 7th Eur. Radar Conf.*, 2010, pp. 89–92.

[4] G. Pyo, C.-Y. Kim, and S. Hong, "Single-antenna FMCW radar CMOS transceiver IC," *IEEE Trans. Microw. Theory Techn.*, vol. 65, no. 3, pp. 945–954, Mar. 2017.

[5] H.-C. Kuo *et al.*, "A fully integrated 60-GHz CMOS direct-conversion Doppler radar RF sensor with clutter canceller for single-antenna noncontact human vital-signs detection," *IEEE Trans. Microw. Theory Techn.*, vol. 64, no. 4, pp. 1018–1028, Apr. 2016.

[6] S. H. Abdelhalem *et al.*, "Tunable CMOS integrated duplexer with antenna impedance tracking and high isolation in the transmit and receive bands," *IEEE Trans. Microw. Theory Techn.*, vol. 62, no. 9, pp. 2092–2104, Sep. 2014.

[7] C. Y. Kim, J. G. Kim, D. Baek, and S. Hong, "A circularly polarized balanced radar front-end with a single antenna for 24-GHz radar applications," *IEEE Trans. Microw. Theory Techn.*, vol. 57, no. 2, pp. 293–297, Feb. 2009.

[8] R. H. Rasshofer and K. Gresser, "Automotive radar and LiDAR systems for next generation driver assistance functions," *Adv. Radio Sci.*, vol. 3, pp. 205–209, May 2005.

[9] Y. Li and J. Ibanez-Guzman, "LiDAR for autonomous driving: The principles, challenges, and trends for automotive LiDAR and perception systems," *IEEE Signal Process. Mag.*, vol. 37, no. 4, pp. 50–61, Jul. 2020.

[10] M. Khader and S. Cherian, "An introduction to automotive LiDAR," Temp. Humidity Sens., High-Speed Amplif., Texas Instrum., Dallas, TX, USA, Tech. Rep., 2018.

[11] M. Kutila, P. Pyykonen, H. Holzhuter, M. Colomb, and P. Duthon, "Automotive LiDAR performance verification in fog and rain," in *Proc. 21st Int. Conf. Intell. Transp. Syst. (ITSC)*, Nov. 2018, pp. 1695–1701.

[12] R. Heinzler, P. Schindler, J. Seekircher, W. Ritter, and W. Stork, "Weather influence and classification with automotive LiDAR sensors," in *Proc. IEEE Intell. Vehicles Symp. (IV)*, Jun. 2019, pp. 1527–1534.

[13] M. Kutila, P. Pyykonen, W. Ritter, O. Sawade, and B. Schaufele, "Automotive LiDAR sensor development scenarios for harsh weather conditions," in *Proc. IEEE 19th Int. Conf. Intell. Transp. Syst. (ITSC)*, Nov. 2016, pp. 265–270.

[14] N. M. Monroe, G. C. Doqiamis, R. Stingel, P. Myers, X. Chen, and R. Han, "Electronic THz pencil beam forming and 2D steering for high angular-resolution operation: A 98×98-unit 265 GHz CMOS reflectarray with in-unit digital beam shaping and squint correction," in *IEEE Int. Solid-State Circuits Conf. (ISSCC) Dig. Tech. Papers*, vol. 65, Feb. 2022, pp. 84–86.

[15] X. Yi, C. Wang, X. Chen, J. Wang, J. Grajal, and R. Han, "A 220-to-320-GHz FMCW radar in 65-nm CMOS using a frequency-comb architecture," *IEEE J. Solid-State Circuits*, vol. 56, no. 2, pp. 327–339, Feb. 2021.

[16] A. Zandieh, S. Bonen, M. S. Dadash, M. J. Gong, J. Hasch, and S. P. Voinigescu, "155 GHz FMCW and stepped-frequency carrier OFDM radar sensor transceiver IC featuring a PLL with <30 ns settling time and 40 fs rms jitter," *IEEE Trans. Microw. Theory Techn.*, vol. 69, no. 11, pp. 4908–4924, Nov. 2021.

[17] A. Visweswaran *et al.*, "A 28-nm-CMOS based 145-GHz FMCW radar: System, circuits, and characterization," *IEEE J. Solid-State Circuits*, vol. 56, no. 7, pp. 1975–1993, Jul. 2021.

[18] W. A. Ahmad *et al.*, "Multimode W-band and D-band MIMO scalable radar platform," *IEEE Trans. Microw. Theory Techn.*, vol. 69, no. 1, pp. 1036–1047, Jan. 2021.

[19] A. Mostajeran, A. Cathelin, and E. Afshari, "A 170-GHz fully integrated single-chip FMCW imaging radar with 3-D imaging capability," *IEEE J. Solid-State Circuits*, vol. 52, no. 10, pp. 2721–2734, Oct. 2017.

[20] H. J. Ng, M. Kucharski, W. Ahmad, and D. Kissinger, "Multi-purpose fully differential 61- and 122-GHz radar transceivers for scalable MIMO sensor platforms," *IEEE J. Solid-State Circuits*, vol. 52, no. 9, pp. 2242–2255, Sep. 2017.

[21] M. Born *et al.*, *Geometrical Theory of Optical Imaging*, 7th ed. Cambridge, U.K.: Cambridge Univ. Press, 1999, pp. 142–227.

[22] M. Pauli *et al.*, "Miniaturized millimeter-wave radar sensor for high-accuracy applications," *IEEE Trans. Microw. Theory Techn.*, vol. 65, no. 5, pp. 1707–1715, Mar. 2017.

[23] N. Pohl, T. Jaeschke, and K. Aufinger, "An ultra-wideband 80 GHz FMCW radar system using a SiGe bipolar transceiver chip stabilized by a fractional-N PLL synthesizer," *IEEE Trans. Microw. Theory Techn.*, vol. 60, no. 3, pp. 757–765, Jan. 2012.

[24] J. Zhou, T.-H. Chuang, T. Dinc, and H. Krishnaswamy, "Integrated wideband self-interference cancellation in the RF domain for FDD and full-duplex wireless," *IEEE J. Solid-State Circuits*, vol. 50, no. 12, pp. 3015–3031, Dec. 2015.

[25] M. Kalantari, H. Shirinabadi, A. Fotowat-Ahmadi, and C. P. Yue, "A single-antenna W-band FMCW radar front-end utilizing adaptive leakage cancellation," in *IEEE Int. Solid-State Circuits Conf. (ISSCC) Dig. Tech. Papers*, Feb. 2020, pp. 88–90.

[26] M. Kucharaski, W. A. Ahmad, H. J. Ng, and D. Kissinger, "Monostatic and bistatic G-band BiCMOS radar transceivers with on-chip antennas and tunable TX-to-RX leakage cancellation," *IEEE J. Solid-State Circuits*, vol. 56, no. 3, pp. 899–913, Mar. 2021.

[27] T. Jaeschke, C. Bredendiek, S. Küppers, and N. Pohl, "High-precision D-band FMCW-radar sensor based on a wideband SiGe-transceiver MMIC," *IEEE Trans. Microw. Theory Techn.*, vol. 62, no. 12, pp. 3582–3597, Dec. 2014.

[28] M. Hitzler, P. Grüner, L. Boehm, W. Mayer, and C. Waldschmidt, "On monostatic and bistatic system concepts for mm-wave radar MMICs," *IEEE Trans. Microw. Theory Techn.*, vol. 66, no. 9, pp. 4204–4215, Sep. 2018.

[29] J. Grzyb, K. Statnikov, N. Sarmah, B. Heinemann, and U. R. Pfeiffer, "A 210–270-GHz circularly polarized FMCW radar with a single-lens-coupled SiGe HBT chip," *IEEE Trans. Terahertz Sci. Technol.*, vol. 6, no. 6, pp. 771–783, Nov. 2016.

[30] X. Chen *et al.*, "A 140 GHz transceiver with integrated antenna, inherent-low-loss duplexing and adaptive self-interference cancellation for FMCW monostatic radar," in *IEEE Int. Solid-State Circuits Conf. (ISSCC) Dig. Tech. Papers*, Feb. 2022, pp. 80–82.

[31] X. Li *et al.*, "A high-efficiency 142–182-GHz SiGe BiCMOS power amplifier with broadband slotline-based power combining technique," *IEEE J. Solid-State Circuits*, vol. 57, no. 2, pp. 371–384, Feb. 2022.

[32] Y.-Y. Huang, H. Jeon, Y. Yoon, W. Woo, C.-H. Lee, and J. S. Kenney, "An ultra-compact, linearly-controlled variable phase shifter designed with a novel RC poly-phase filter," *IEEE Trans. Microw. Theory Techn.*, vol. 60, no. 2, pp. 301–310, Feb. 2012.

[33] J. Zhu *et al.*, “Additively manufactured millimeter-wave dual-band single-polarization shared aperture Fresnel zone plate metalens antenna,” *IEEE Trans. Antennas Propag.*, vol. 69, no. 10, pp. 6261–6272, Oct. 2021.

[34] S. M. Patole, M. Torlak, D. Wang, and M. Ali, “Automotive radars: A review of signal processing techniques,” *IEEE Signal Process. Mag.*, vol. 34, no. 2, pp. 22–35, Mar. 2017.

Xibi Chen (Student Member, IEEE) received the B.S. and M.S. degrees from Tsinghua University, Beijing, China, in 2017 and 2020, respectively. He is currently pursuing the Ph.D. degree with the Department of Electrical Engineering and Computer Science (EECS), Massachusetts Institute of Technology (MIT), Cambridge, MA, USA.

From 2015 to 2017, he was a Research Assistant with the Department of Electronic Engineering, Microwave and Antenna Institute, Tsinghua University, where he later became a Graduate Student Researcher from 2017 to 2019. In 2020, he joined EECS, MIT, as a Ph.D. Student. His current research interests include terahertz (THz) integrated electronic systems, THz imaging/sensing, and CMOS electromagnetics/optics.

Mr. Chen was a recipient of the ISSCC 2022 Student Travel Grant Award and the Analog Devices Outstanding Student Designer Award.

Xiang Yi (Senior Member, IEEE) received the B.E. degree from the Huazhong University of Science and Technology (HUST), Wuhan, China, in 2006, the M.S. degree from the South China University of Technology (SCUT), Guangzhou, China, in 2009, and the Ph.D. degree from Nanyang Technological University (NTU), Singapore, in 2014.

He is currently a Professor with SCUT. Before that, he was a Post-Doctoral Fellow with the Massachusetts Institute of Technology (MIT), Cambridge, MA, USA. His research interests include radio frequency (RF), millimeter-wave (mm-wave), and terahertz (THz)-frequency synthesizers and transceiver systems.

Dr. Yi was a recipient of the IEEE ISSCC Silkroad Award and the SSCS Travel Grant Award in 2013. He is a technical reviewer for several IEEE journals and conferences.

Muhammad Ibrahim Wasiq Khan (Student Member, IEEE) received the B.E. degree (Hons.) in electrical engineering from the National University of Science and Technology (NUST), Islamabad, Pakistan, in 2012, and the M.Sc. degree in electrical engineering from the Korea Advanced Institute of Science and Technology (KAIST), Daejeon, South Korea, in 2016. He is currently pursuing the Ph.D. degree with the Department of Electrical Engineering and Computer Science (EECS), Massachusetts Institute of Technology (MIT), Cambridge, MA, USA, with a focus on CMOS-based terahertz (THz) identification tags, THz energy-harvesting systems, and THz-orbital-angular-momentum (OAM) secure transceivers.

He worked on THz detectors and THz imaging systems based on CMOS technology at KAIST. His research interests include mm-wave and THz integrated wireless systems.

Mr. Khan was awarded the IEEE Microwave Theory and Techniques Society (MTT-S) Graduate Fellowship in 2022. He was a recipient of the IEEE Radio-Frequency Integrated Circuits (RFIC) Symposium Best Student Paper Award (First Place) in 2021. He also received the Rector’s Silver Medal for his B.E. degree.

Xingcun Li (Student Member, IEEE) received the B.S. degree in electronic information science and technology from the University of Electronic Science and Technology of China (UESTC), Chengdu, China, in 2017. He is currently pursuing the Ph.D. degree with the Department of Electronic Engineering, Tsinghua University, Beijing, China.

In 2020, he was a Visiting Student with the Department of Electrical Engineering and Computer Science, Massachusetts Institute of Technology (MIT), Cambridge, MA, USA. His current research interests include silicon-based mm-wave and THz integrated circuits for radar and wireless communication.

Wenhua Chen (Senior Member, IEEE) received the B.S. degree in microwave engineering from the University of Electronic Science and Technology of China (UESTC), Chengdu, China, in 2001, and the Ph.D. degree in electronic engineering from Tsinghua University, Beijing, China, in 2006.

From 2010 to 2011, he was a Post-Doctoral Fellow with iRadio Laboratory, University of Calgary, Calgary, AB, Canada. He is currently a Full Professor with the Department of Electronic Engineering, Tsinghua University. He has authored or coauthored over 200 journal articles and conference papers. His main research interests include energy-efficient power amplifiers (PA) and linearization, and millimeter-wave integrated circuits.

Dr. Chen was a recipient of the 2015 Outstanding Youth Science Foundation of NSFC, the 2014 URSI Young Scientist Award, and the Student Paper Awards of several international conferences. He is currently an Associate Editor of IEEE MICROWAVE AND WIRELESS COMPONENTS LETTERS and an Editorial Member of *Engineering*. He was an Associate Editor of the IEEE TRANSACTIONS ON MICROWAVE THEORY AND TECHNIQUES.

Jianfeng Zhu (Student Member, IEEE) was born in Changsha, China. He received the B.E. degree in communication engineering from the Beijing University of Posts and Telecommunications (BUPT), Beijing, China, in 2013, and joint Ph.D. degree from BUPT and the University of Technology Sydney (UTS), Ultimo, NSW, Australia, in 2021.

From November 2015 to June 2018, he was a Research Assistant with the State Key Laboratory of Millimeter Waves, Department of Electronic Engineering, City University of Hong Kong, Hong Kong. He has authored and coauthored more than 40 journal articles and conference papers.

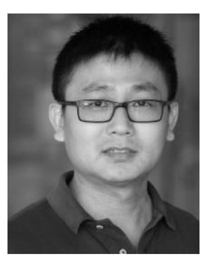

Yang Yang (Senior Member, IEEE) was born in Bayannur, Inner Mongolia, China. He received the Ph.D. degree in electronic engineering from Monash University, Clayton Campus, Melbourne, VIC, Australia, in 2013.

He worked for Rain Bird Australia, Deer Park, VIC, Australia, from 2012 to 2015. In April 2015, he returned to academia and served as a Senior Research Associate at Macquarie University, Sydney, VIC, Australia. In April 2016, he was appointed as a Research Fellow with the State Key Laboratory of Terahertz and Millimeter Waves, City University of Hong Kong, Hong Kong. He is currently a Senior Lecturer and the Group Leader of the Millimeter-Wave and Terahertz Circuits and Antennas. He has published one book, two book chapters, and over 200 international peer-reviewed journal articles and conference papers. His research interests include 3-D printing, millimeter-wave, and sub-terahertz technologies in 5G and biomedical applications.

Dr. Yang received the Linkage Infrastructure, Equipment and Facilities (LIEF) Award funded by the Australian Research Council to establish the Australian 3D Terahertz Beam Measurement Platform in 2021. He received the 2014 Global GSP Success Award by Rain Bird Corporation, Tucson, USA. He was the winner of the CST University Publication Award 2018, by CST, Dassault Systèmes.

Kenneth E. Kolodziej (Senior Member, IEEE) received the B.E. and M.E. degrees in electrical engineering from the Stevens Institute of Technology, Hoboken, NJ, USA, in 2007.

In 2007, he joined BAE Systems, Wayne, NJ, to design RF electronics for handheld communication devices. Since 2010, he has been working with the MIT Lincoln Laboratory, Lexington, MA, USA, and has conducted research on RF, microwave, and photonic circuits, including antenna, radar, and communications systems. He is currently a Principal Investigator with the Advanced Technology Division's RF Technology Group, leading teams designing cancellation techniques and systems for in-band full-duplex applications. He also holds a Lecturer position with the MIT Department of Electrical Engineering and Computer Science, where he has taught an undergraduate electromagnetics course and several "Build-a-Radar" courses on the MIT campus.

Mr. Kolodziej was a Guest Editor of the IEEE TRANSACTIONS ON MICROWAVE THEORY AND TECHNIQUES. He is an Editor of the *In-Band Full-Duplex Wireless Systems Handbook* (Artech House) and an Associate Editor of the *IEEE Microwave Magazine* since 2021. He is a member of the IEEE MTT-S Wireless Communications (MTT-23) Technical Committee. He has been a member of the technical program committees of several conferences, including the IEEE International Microwave Symposium since 2019; the IEEE Radio & Wireless Symposium since 2022; the IEEE International Symposium on Antennas and Propagation since 2017; the IEEE International Symposium on Phased Array Systems and Technology since 2019; and the IEEE International Conference on Communications since 2020.

Nathan M. Monroe (Student Member, IEEE) received the B.S., M.Eng., and Ph.D. degrees in electrical engineering from the Massachusetts Institute of Technology (MIT), Cambridge, MA, USA, in 2013, 2017, and 2022, respectively.

From 2013 to 2015, he worked on the Xbox Hardware Development Team at Microsoft, Redmond, WA, USA, where he focused on sensor arrays and time of flight imaging. His Ph.D. thesis focused on high directivity terahertz antenna arrays for real-time imaging applications. His research interests include terahertz circuits and systems, imaging radar, and metamaterials.

Ruonan Han (Senior Member, IEEE) received the B.Sc. degree in microelectronics from Fudan University, Shanghai, China, in 2007, the M.Sc. degree in electrical engineering from the University of Florida, Gainesville, FL, USA, in 2009, and the Ph.D. degree in electrical and computer engineering from Cornell University, Ithaca, NY, USA, in 2014.

He is currently a tenured Associate Professor with the Department of Electrical Engineering and Computer Science, Massachusetts Institute of Technology, Cambridge, MA, USA. His research interests include microelectronic circuits and systems operating at millimeter-wave and terahertz frequencies.

Dr. Han was a recipient of the Cornell ECE Director's Ph.D. Thesis Research Award, the Cornell ECE Innovation Award, the IEEE Microwave Theory and Techniques Society (MTT-S) Graduate Fellowship Award, the IEEE Solid-State Circuits Society (SSC-S) Predoctoral Achievement Award, the Intel Outstanding Researcher Award in 2019, and the U.S. National Science Foundation (NSF) CAREER Award in 2017. He and his students won three Best Student Paper Awards at the IEEE Radio-frequency Integrated Circuits (RFIC) Symposium (2012, 2017, and 2021). He serves/served as an Associate Editor for IEEE TRANSACTIONS ON VERY LARGE SCALE INTEGRATION (VLSI) SYSTEMS (2019–2021), IEEE TRANSACTIONS ON MICROWAVE THEORY AND TECHNIQUES (2019), and IEEE TRANSACTIONS ON QUANTUM ENGINEERING (since 2020). He is/was also on the Technical Program Committees of the IEEE International Solid-State Circuits Conference (ISSCC) and IEEE RFIC Symposium and the Steering Committee of the IEEE International Microwave Symposium (IMS). He is an IEEE MTT-S Distinguished Lecturer for the term 2020–2022.